Geochemistry, Geophysics, Geosystems®

RESEARCH ARTICLE
10.1029/2022GC010807

Key Points:

- An exact solution is manufactured for a realistic thermochemical mantle convection flow in two dimensions
- An exact solution is highly useful for software verification and validation for problems featuring sharply varying thermochemical flows
- Maple™ is used to assist with symbolic computations, and the resulting formulas are also provided in Fortran and Python

Correspondence to:
S. J. Trim,
sean.trim@usask.ca

Citation:
Trim, S. J., Butler, S. L., McAdam, S. S. C., & Spiteri, R. J. (2023). Manufacturing an exact solution for 2D thermochemical mantle convection models. *Geochemistry, Geophysics, Geosystems*, *24*, e2022GC010807. https://doi.org/10.1029/2022GC010807

Received 28 NOV 2022
Accepted 25 MAR 2023

Author Contributions:
Conceptualization: S. J. Trim, R. J. Spiteri
Data curation: S. J. Trim
Formal analysis: S. J. Trim, S. L. Butler, R. J. Spiteri
Funding acquisition: S. L. Butler, R. J. Spiteri
Investigation: S. J. Trim, S. L. Butler
Methodology: S. J. Trim, R. J. Spiteri
Project Administration: R. J. Spiteri
Resources: S. S. C. McAdam, R. J. Spiteri
Software: S. J. Trim, S. S. C. McAdam
Supervision: S. J. Trim, R. J. Spiteri
Validation: S. J. Trim

Manufacturing an Exact Solution for 2D Thermochemical Mantle Convection Models

S. J. Trim[1], S. L. Butler[2], S. S. C. McAdam[1], and R. J. Spiteri[1]

[1]Department of Computer Science, University of Saskatchewan, Saskatoon, SK, Canada, [2]Department of Geological Sciences, University of Saskatchewan, Saskatoon, SK, Canada

Abstract In this study, we manufacture an exact solution for a set of 2D thermochemical mantle convection problems. The derivation begins with the specification of a stream function corresponding to a non-stationary velocity field. The method of characteristics is then applied to determine an expression for composition consistent with the velocity field. The stream function formulation of the Stokes equation is then applied to solve for temperature. The derivation concludes with the application of the advection-diffusion equation for temperature to solve for the internal heating rate consistent with the velocity, composition, and temperature solutions. Due to the large number of terms, the internal heating rate is computed using Maple™, and code is also made available in Fortran and Python. Using the method of characteristics allows the compositional transport equation to be solved without the addition of diffusion or source terms. As a result, compositional interfaces remain sharp throughout time and space in the exact solution. The exact solution presented allows for precision testing of thermochemical convection codes for correctness and accuracy.

Plain Language Summary We manufacture an exact solution for a set of 2D thermochemical mantle convection problems, for which both thermal and compositional gradients impact buoyancy. Such problems must typically be solved approximately via computer models and are notoriously difficult to solve accurately. Our derivation uses a mathematical technique known as the method of characteristics that allows us to solve for composition and temperature variables without adding artificial terms to the model equations. Accordingly, our solution is able to feature sharp compositional gradients, which are difficult to model numerically. The exact solution facilitates the testing of thermochemical convection codes for both correctness and accuracy.

1. Introduction

1.1. Motivation

Buoyancy is the primary driving force behind convection in the Earth's mantle. Contributing factors to buoyancy in the mantle include lateral contrasts in temperature and composition. In the case of thermochemical flows, mantle buoyancy depends upon both of these factors. Heat sources and sinks affecting the thermal state of the Earth's mantle include radiogenic heating, heating from the outer core, and cooling at the Earth's surface (Turcotte & Schubert, 2002). Thermally driven buoyancy instabilities can arise when the rate of thermal transport via advection exceeds that of diffusion. Such situations include the rise of hot upwellings from the core and the descent of cold downwellings from the surface (e.g., a subducting slab). Buoyancy instabilities can also be caused by lateral variations in thermal boundary conditions. Lateral contrasts in mantle composition can occur for several reasons, including transitions between oceanic and continental lithosphere, rapid subduction of oceanic lithosphere, and deep dense compositional piles. The Earth's Large Low Shear wave Velocity Provinces may also be influenced by thermal and compositional gradients (Davies et al., 2015; McNamara, 2019).

Geophysical flows involving sharp compositional contrasts are notoriously difficult to model numerically. Challenges include both spurious oscillations and extraneous diffusion (Lenardic & Kaula, 1993). Numerical methods employed to minimize these errors include the use of particles (Tackley & King, 2003), level sets (Hillebrand et al., 2014), and hybrid methods (Samuel & Evonuk, 2010).

Another even more fundamental challenge is to ensure the software that implements the numerical solution has been coded correctly. By definition, model developers produce code to solve problems for which solutions are unknown. The verification and validation process in modeling and simulation often involves qualitative

Visualization: S. J. Trim, S. S. C. McAdam
Writing – original draft: S. J. Trim, S. L. Butler, R. J. Spiteri
Writing – review & editing: S. J. Trim, S. L. Butler, R. J. Spiteri

comparison with accepted published results or quantitative comparison with a highly accurate "reference solution." In the latter case, it can be questionable practice to use one's own software for verification purposes, or it potentially forces the developers to learn and use other software. Accordingly, the presence of an exact solution with which numerical solutions can be compared is highly desirable, especially if it is realistic. In this paper, we describe a realistic 2D thermochemical mantle convection problem for which we manufacture an exact solution.

1.2. Solution Features

Exact solutions applicable to mantle convection codes have been presented for situations including Stokes flow with lateral viscosity variations (Duretz et al., 2011; Pusok et al., 2017; Samuel, 2018; Zhong, 1996), material deformation (Enright et al., 2002), and compositional convection (Gassmöller et al., 2019). However, our manufactured solution includes both thermal and compositional buoyancy effects, has a non-stationary velocity field (Brunton & Rowley, 2010), and does not require the addition of source or diffusion terms in the compositional transport equation. We believe that the inclusion of these features brings the problem closer to practical thermochemical mantle convection models and allows for a greater range of numerical testing. For instance, having a combination of thermal and compositional buoyancy effects allows testing the numerical accuracy of the correlation between temperature and composition over a range of buoyancy ratios. Further, a non-stationary velocity field allows for testing the efficacy of numerical schemes for temporally variable velocity fields.

Additionally, deriving an exact solution without requiring compositional sources, sinks, or diffusion ensures that compositional contrasts remain sharp, which is typically the desired behavior in mantle convection studies. To accomplish this, we employ the method of characteristics (Courant & Hilbert, 2008) for the analysis of compositional transport. The method of characteristics has been previously applied to enhance the numerical techniques for modeling compositional transport in geodynamic flows (De Smet et al., 2000; Gerya & Yuen, 2003). In this study, we focus on applying the method of characteristics to facilitate an exact solution to the compositional transport problem.

1.3. Derivation Outline

The primary steps of the derivation are as follows:

1. Prescribe a stream function that varies in time and space and corresponds to a velocity field that is reasonable for mantle convection.
2. Apply the method of characteristics to find the time-dependent solution for the composition field that matches the stream function.
3. Solve for the temperature given the stream function and the composition field by applying the stream function formulation of the Stokes equation.
4. Determine the internal heating rate that corresponds to the stream function, temperature, and composition fields using the advection-diffusion equation governing temperature.

The remainder of this paper provides details of the steps just described in the context of a rectangular 2D domain with specific initial conditions, boundary conditions, and stream function to yield a realistic velocity field. We note that the use of a prescribed stream function to study compositional convection has been used previously (Kellogg & Turcotte, 1990).

2. Method

2.1. Governing Equations

Although effectively solid over short time periods, the mantle acts as a highly viscous fluid over geologic time (Schubert et al., 2001). Mathematically, the mantle is typically modeled using a set of conservation equations obtained from fluid dynamics and thermodynamics. Specifically, the continuity equation specifies the conservation of mass, the Navier–Stokes equation models the conservation of momentum, and an advection-diffusion equation governs the conservation of energy. In addition, an advection equation is used to model compositional transport of distinct mantle components. We employ the Boussinesq approximation to simplify the effect of density variations. The infinite Prandtl number approximation is also used, for which the inertial terms in the Navier–Stokes equation are considered negligible (resulting in Stokes flow).

In the case of 2D incompressible flow in Cartesian coordinates, we may use the stream function formulation to simplify the treatment of the conservation of mass and momentum. Specifically, the non-dimensional biharmonic equation, given by

$$\frac{\partial^4\psi}{\partial x^4} + \frac{\partial^4\psi}{\partial x^2\partial z^2} + \frac{\partial^4\psi}{\partial z^4} = Ra_T\frac{\partial T}{\partial x} - Ra_C\frac{\partial C}{\partial x}, \tag{1}$$

may be used, where ψ is the stream function; T and C are the temperature and composition fields; x and z are the horizontal and vertical (increasing opposite to the direction of gravity) position coordinates; and Ra_T and Ra_C are the thermal and compositional Rayleigh numbers (Batchelor, 1967; van Keken et al., 1997). We note that Equation 1 is the isoviscous form of the biharmonic equation. In principle, it is possible to include viscosity variations in the following derivation of a manufactured solution. However, this complicates the symbolic computations required to find formulas for the temperature and internal heating rate. Accordingly, we leave the inclusion of variable viscosity for a future study.

The velocity ($\mathbf{v}$) is computed from the stream function using

$$\mathbf{v} = (u, w) = \left(\frac{\partial\psi}{\partial z}, -\frac{\partial\psi}{\partial x}\right), \tag{2}$$

where u and w are the horizontal and vertical velocity components, respectively. We note that Equation 2 yields a velocity that is inherently divergence free. The stream function formulation reduces the number of scalar equations to be solved and removes the need to solve for the pressure, at the expense, however, of solving a higher-order equation.

The non-dimensional conservation equations for energy and composition are

$$\frac{\partial T}{\partial t} + \mathbf{v}\cdot\nabla T = \nabla^2 T + H, \tag{3}$$

and

$$\frac{\partial C}{\partial t} + \mathbf{v}\cdot\nabla C = 0, \tag{4}$$

respectively, where H is the internal heating rate and t is time.

The thermal Rayleigh number is

$$Ra_T = \frac{\alpha\rho_0 g\,\delta T\,L^3}{\kappa\eta_0}, \tag{5}$$

where α is the thermal expansivity; ρ_0 is surface density with $C = T = 0$; g is the gravitational acceleration; δT is the temperature difference across the mantle; L is the mantle thickness; κ is thermal diffusivity; and η_0 is the surface viscosity. The compositional Rayleigh number is

$$Ra_C = \frac{\delta\rho_C\,g\,L^3}{\kappa\eta_0}, \tag{6}$$

where $\delta\rho_C$ is the compositional density contrast between enriched and ambient mantle materials.

2.2. Problem Setup

2.2.1. Problem Domain and Initial Conditions

We assume a problem domain $[0, \lambda] \times [0, 1]$ in the x-z plane, where $\lambda > 0$ is the aspect ratio of the convecting cell.

We require initial conditions for both composition and temperature. For composition, we select a two-layer initial state with a sharp contrast between layers that we denote by $C(x, z, t = 0) = C_0(z)$. In principle, this initial state may be achieved using $C_0(z) = \mathcal{H}\left(\frac{1}{2} - z\right)$, where $\mathcal{H}(\cdot)$ is the Heaviside function. However, we assume that the

compositional interface be of non-zero thickness (see Section 4.3), which is accomplished using the logistic function as a smooth approximation to the Heaviside function

$$C_0(z) = \left[1 + \exp[-2k(z_I - z)]\right]^{-1}, \tag{7}$$

where k controls the sharpness of the interface at $z = z_I$. For temperature, we have

$$T(x, z, t = 0) = \frac{1}{Ra_T}\left[-\frac{\pi^3\left(\lambda^2 + 1\right)^2}{\lambda^3}\cos(\pi x/\lambda)\sin(\pi z) f(t = 0) + Ra_C C_0(z) + (Ra_T - Ra_C)(1 - z)\right], \tag{8}$$

which is a hybrid between a conductive and layered profile (with layers corresponding to the initial composition field), with a sinusoidal perturbation. The perturbation is scaled by the initial value of the function $f(t)$, which controls the time dependence of the presumed ψ (see Section 3.1.1). This particular initial condition for T was chosen to simplify the treatment of internal heating in the derivation. However, other choices, such as a purely conductive profile, are possible with the appropriate choice of $f_B(z, t)$ in Equation 43 below (see Section 3.1 for details).

We note that the above initial conditions for C and T imply stable buoyancy for $t = 0$. For our problem, convection is initiated by lateral gradients in the internal heating rate (see Section 3.1.5).

2.2.2. Boundary Conditions

To form a well-posed problem, boundary conditions are required for temperature and the velocity field. Our goal in selecting boundary conditions is to match realistic mantle convection models as closely as possible. For temperature, we select insulating sidewalls ($\partial T/\partial x = 0$ at $x = 0$ and $x = \lambda$) and isothermal horizontal boundaries, $T(x, z = 0, t) = T_{\text{bot}}$ and $T(x, z = 1, t) = T_{\text{top}}$), where

$$T_{\text{bot}} = \frac{Ra_C}{Ra_T}[C_0(0) - 1] + 1 \tag{9}$$

and

$$T_{\text{top}} = \frac{Ra_C}{Ra_T}C_0(1). \tag{10}$$

The values of T_{bot} and T_{top} were selected to simplify the derivation of T and are consistent with the initial condition. Note that T_{bot} and T_{top} approach values of unity and zero, respectively, as the value of k increases. With these boundary conditions, the flow is characterized by mixed heating modes: basal and internal. For the velocity field, we choose impermeable ($u = 0$ at $x = 0$ and $x = \lambda$, $w = 0$ at $z = 0$ and $z = 1$) and free-slip ($\partial u/\partial z = 0$ at $z = 0$ and $z = 1$, $\partial w/\partial x = 0$ at $x = 0$ and $x = \lambda$) boundaries. Note that boundary fluxes of composition are zero due to the use of impermeable boundary conditions for velocity.

2.2.3. Diagnostics

The root-mean-square (RMS) velocity over the problem domain is defined as

$$v_{\text{RMS}} = \sqrt{\frac{1}{\lambda}\int_0^1\int_0^\lambda \left[u^2 + w^2\right] dx dz} \tag{11}$$

and characterizes the overall vigor of convection. The entrainment is given by

$$E = \frac{1}{\lambda z_I}\int_{z_R}^1\int_0^\lambda C\, dx dz, \tag{12}$$

which quantifies the proportion of material with $C = 1$ above a reference height of z_R. In this study, we use $z_R = z_I$. These quantities have been used to help quantify the accuracy of numerical solutions in thermochemical convection studies (Samuel & Evonuk, 2010; Tackley & King, 2003; S. J. Trim et al., 2020, 2021; van Keken et al., 1997). We report the RMS velocity and entrainment for the manufactured solution in Section 3.2.

3. Results

3.1. Derivation of the Manufactured Solution

We proceed with our derivation of the manufactured solution by finding the shape of the characteristic orbitals for a presumed stream function, followed by determining the time evolution along those orbitals. The method of characteristics can then be applied to find the solution for composition expressed as a transformation of its initial condition. The solution for temperature is then found from the biharmonic equation. Finally, the internal heating rate for this problem is found from the advection-diffusion equation for temperature.

3.1.1. Establishing the Characteristic Orbitals

Equation 4 can be expressed in 2D Cartesian coordinates as

$$\frac{\partial C}{\partial t} + u\frac{\partial C}{\partial x} + w\frac{\partial C}{\partial z} = 0. \tag{13}$$

We seek to describe the evolution of a characteristic curve with coordinates $x(t)$ and $z(t)$. Along this characteristic, we have $C = C(x(t), z(t), t)$ with time derivative given by

$$\frac{dC}{dt} = \frac{\partial C}{\partial x}\frac{dx}{dt} + \frac{\partial C}{\partial z}\frac{dz}{dt} + \frac{\partial C}{\partial t}. \tag{14}$$

Comparing Equations 13 and 14, we extract a system of characteristic ODEs,

$$\begin{cases} dx/dt = u, \\ dz/dt = w, \\ dC/dt = 0. \end{cases} \tag{15}$$

Because $dC/dt = 0$ along a characteristic, we have $C(x(t), z(t), t) = C(x_0, z_0, 0)$, where $x_0 = x(0)$ and $z_0 = z(0)$. If we can solve for x_0 and z_0 in terms of $x(t)$, $z(t)$, and t, we can obtain the exact time-dependent solution for C.

To obtain a suitable velocity field, we assume a stream function that satisfies the boundary conditions (see Section 2.2.2) and is given by

$$\psi(x, z, t) = \sin(\pi x/\lambda)\sin(\pi z)f(t), \tag{16}$$

where $f(t)$ is an integrable function of time. Using Equation 2 in conjunction with Equation 15, we obtain the characteristic ODEs governing the trajectories $x(t)$ and $z(t)$, namely

$$\begin{cases} dx/dt = \pi\sin(\pi x/\lambda)\cos(\pi z)f(t), \\ dz/dt = -\dfrac{\pi}{\lambda}\cos(\pi x/\lambda)\sin(\pi z)f(t). \end{cases} \tag{17}$$

Dividing equations and rearranging gives

$$\frac{1}{\lambda}\cot(\pi x/\lambda)dx = -\cot(\pi z)dz. \tag{18}$$

Integrating both sides of Equation 18 gives

$$\frac{1}{\lambda}\left[\frac{\lambda}{\pi}\ln|\sin(\pi x/\lambda)| + D_1\right] = -\left[\frac{1}{\pi}\ln|\sin(\pi z)| + D_2\right], \tag{19}$$

where D_1 and D_2 are constants of integration. Rearranging terms and applying the properties of logarithms gives

$$\ln|\sin(\pi x/\lambda)\sin(\pi z)| = -\pi(D_1/\lambda + D_2). \tag{20}$$

Exponentiating both sides results in

$$|\sin(\pi x/\lambda)\sin(\pi z)| = D, \tag{21}$$

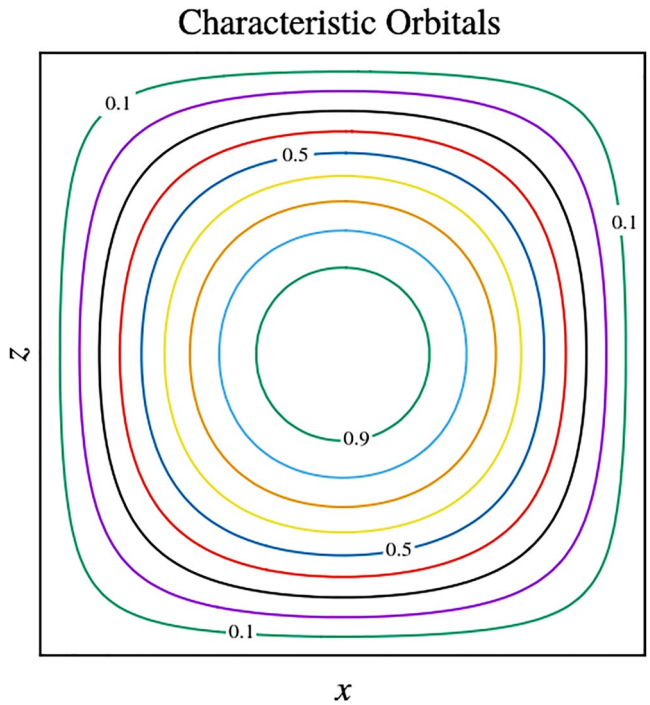

Figure 1. Sample contours of D, corresponding to characteristic orbitals, from Equation 21 with $\lambda = 1$. Contour values range between 0.1 and 0.9 and are shown at intervals of 0.1. The value of D increases toward a value of unity at the center of the domain.

where $D \equiv \exp[-\pi(D_1/\lambda + D_2)]$ is a constant. Sample contours of D for $\lambda = 1$, corresponding to characteristic orbital trajectories, are shown in Figure 1. For the characteristics corresponding to a given value of D, Equation 21 gives us the shape of the orbital path. However, we still need to determine the time dependence of the evolution of the characteristics to complete the solution.

3.1.2. Time Evolution of Characteristics Corresponding to $0 < D < 1$

The initial condition for C consists of horizontal layers. Accordingly, Equation 7 is independent of x, and we need only analyze the time dependence of z as governed by dz/dt in Equation 17. Consequently, we must eliminate the $\cos(\pi x/\lambda)$ term from dz/dt in Equation 17. The Pythagorean identity gives

$$\cos(\pi x/\lambda) = S(x)\sqrt{1 - \sin^2(\pi x/\lambda)}, \tag{22}$$

where the function $S(x)$ is defined by

$$S(x) = \begin{cases} +1 & \text{if } x \le \lambda/2, \\ -1 & \text{if } x > \lambda/2, \end{cases} \tag{23}$$

and is used to ensure the correct sign for the cosine function about $x = \lambda/2$. Using Equation 21 in Equation 22, we obtain

$$\cos(\pi x/\lambda) = S(x)\sqrt{1 - \frac{D^2}{\sin^2(\pi z)}}. \tag{24}$$

Substitution of Equation 24 into Equation 17 for dz/dt gives

$$\begin{aligned} \frac{dz}{dt} &= -\frac{\pi}{\lambda} f(t) S(x) \sqrt{\sin^2(\pi z) - D^2} \\ &= -\frac{\pi}{\lambda} f(t) S(x) (\pm i D) \sqrt{1 - \frac{1}{D^2}\sin^2(\pi z)} \\ &= \frac{i\pi D}{\lambda} f(t) S(x) \sqrt{1 - \frac{1}{D^2}\sin^2(\pi z)}, \end{aligned} \tag{25}$$

where we have retained the negative of the plus-minus sign to preserve the sign of the vertical velocity component. Rearranging Equation 25 and multiplying both sides by π gives

$$\frac{d(\pi z)}{\sqrt{1 - \frac{1}{D^2}\sin^2(\pi z)}} = \frac{i\pi^2 D}{\lambda} f(t) S(x) dt. \tag{26}$$

Integrating Equation 26 along a particular characteristic, we obtain

$$\int_{\pi z_0}^{\pi z} \frac{d(\pi z)}{\sqrt{1 - \frac{1}{D^2}\sin^2(\pi z)}} = \frac{i\pi^2 D}{\lambda} \int_0^t f(t') S(x) dt', \tag{27}$$

where we have used t' to indicate the dummy variable of integration for time. We may evaluate the left side of Equation 27 in terms of incomplete elliptic integrals of the first kind, giving

$$F\left(\pi z \middle| \frac{1}{D^2}\right) - F\left(\pi z_0 \middle| \frac{1}{D^2}\right) = \frac{i\pi^2 D}{\lambda} \int_0^t f(t') S(x) dt'. \tag{28}$$

We note that the left side only depends on the values of z_0 and z along a characteristic orbital corresponding to the value of D (for $0 < D < 1$). Importantly, the value of the left side does not depend on the path taken along the orbital between the vertical positions of z_0 and z. Accordingly, we may simplify the integral on the right side by selecting paths $x(t)$ along which the function $S(x)$ does not change sign. However, for $x \neq \lambda/2$, each z value

corresponds to two possible x values (one on either side of $x = \lambda/2$, as seen in Figure 1). To account for all possible situations, we select two paths with x ranges given by: (a) $x \leq \lambda/2$ and (b) $x > \lambda/2$. Path 1 starts with $x_0 < \lambda/2$, ends with $x \leq \lambda/2$, and has $x(t) \leq \lambda/2$ for the entire range of integration:

$$F\left(\pi z\middle|\frac{1}{D^2}\right) - F\left(\pi z_0\middle|\frac{1}{D^2}\right) = \frac{i\pi^2 D}{\lambda}\int_0^t f\left(t'\right)dt'. \tag{29}$$

We note that this formula also applies for any case for which $x \leq \lambda/2$. Path 2 starts with $x_0 > \lambda/2$, ends with $x > \lambda/2$, and has $x(t) > \lambda/2$ for the entire range of integration:

$$F\left(\pi z\middle|\frac{1}{D^2}\right) - F\left(\pi z_0\middle|\frac{1}{D^2}\right) = \frac{i\pi^2 D}{\lambda}\int_0^t -f\left(t'\right)dt'. \tag{30}$$

We note that this formula also applies for any case for which $x > \lambda/2$.

Isolating the z_0 terms for all cases, we obtain

$$\begin{aligned} F\left(\pi z_0\middle|\frac{1}{D^2}\right) &= \begin{cases} F\left(\pi z|\frac{1}{D^2}\right) - \frac{i\pi^2 D}{\lambda}\int_0^t f(t')dt', & \text{if } x \leq \lambda/2, \\ F\left(\pi z|\frac{1}{D^2}\right) + \frac{i\pi^2 D}{\lambda}\int_0^t f(t')dt', & \text{if } x > \lambda/2, \end{cases} \\ &= F\left(\pi z\middle|\tfrac{1}{D^2}\right) - S(x)\tfrac{i\pi^2 D}{\lambda}\int_0^t f(t')dt'. \end{aligned} \tag{31}$$

We may use the Jacobi elliptic function cn to extract the cosine of the elliptic amplitude, giving

$$\cos(\pi z_0) = \mathrm{cn}\left\{F\left(\pi z\middle|\frac{1}{D^2}\right) - S(x)\frac{i\pi^2 D}{\lambda}\int_0^t f\left(t'\right)dt'\middle|\frac{1}{D^2}\right\}. \tag{32}$$

Finally, taking the inverse cosine gives

$$z_0 = \frac{1}{\pi}\arccos\left[\mathrm{cn}\left\{F\left(\pi z\middle|\frac{1}{D^2}\right) - S(x)\frac{i\pi^2 D}{\lambda}\int_0^t f\left(t'\right)dt'\middle|\frac{1}{D^2}\right\}\right]. \tag{33}$$

Equation 33 applies to all characteristics for $0 < D < 1$. This covers the majority of the domain, but it does not include the domain boundaries ($D = 0$) nor the center of the domain ($D = 1$). These two special cases for D are now addressed.

3.1.3. Time Evolution of Characteristics for $D = 0$ and $D = 1$

For $D = 0$, the characteristic orbital overlaps with the boundary of the domain. For the horizontal boundaries ($z = 0, 1$), impermeability requires that $z_0 = z$. For the vertical boundaries ($x = 0, \lambda$), Equation 25 gives

$$\begin{aligned} \frac{dz}{dt} &= -\frac{\pi}{\lambda}f(t)S(x)\sqrt{\sin^2(\pi z) - D^2} \\ &= -\frac{\pi}{\lambda}f(t)S(x)|\sin(\pi z)|. \end{aligned} \tag{34}$$

Rearranging terms and integrating both sides gives

$$\int_{z_0}^{z}\csc(\pi z)dz = -\frac{\pi}{\lambda}\int_0^t f\left(t'\right)S(x)dt'. \tag{35}$$

We are able to drop the absolute value sign for the left-hand integrand due to the range of z. Also, the value of x along the vertical boundaries, denoted by x_b, is either 0 or λ. Accordingly, $x = x_b$ is constant in the right-hand integrand, and $S(x_b)$ can be brought outside of the integral. After integrating and isolating terms that depend on z_0, we obtain

$$\begin{aligned} \ln|\csc(\pi z_0) + \cot(\pi z_0)| &= \ln|\csc(\pi z) + \cot(\pi z)| - \frac{\pi}{\lambda}S(x_b)\int_0^t f\left(t'\right)dt' \\ &\equiv Q(z,t), \end{aligned} \tag{36}$$

where we use $Q(z, t)$ to represent the right side of the equation to simplify the notation that follows. To solve Equation 36 for $z_0 = z_0(z, t)$, we make use of the substitution $Z_0 = \cot(\pi z_0)$. For computational convenience, we presume a range of $(-\pi/2, \pi/2] - \{0\}$ for the corresponding inverse cotangent function, which will be used to recover z_0. Taking the exponential of both sides of Equation 36 and applying the Z_0 substitution gives

$$\begin{aligned} e^Q &= |\csc(\pi z_0) + \cot(\pi z_0)| \\ &= |\pm\sqrt{1 + Z_0^2} + Z_0|, \end{aligned} \tag{37}$$

where the plus-minus sign is positive for $Z_0 \geq 0$ and negative for $Z_0 < 0$. Equation 37 has the admissible solution

$$Z_0 = -\frac{1}{2}\left[e^{-Q} - e^Q\right]. \tag{38}$$

Accordingly, for $D = 0$ at the sidewalls, we have

$$z_0 = \begin{cases} \frac{1}{\pi}\operatorname{arccot}(Z_0), & \text{if } Z_0 \geq 0, \\ 1 + \frac{1}{\pi}\operatorname{arccot}(Z_0), & \text{if } Z_0 < 0. \end{cases} \tag{39}$$

For $D = 1$ in the problem domain, examination of Equation 21 reveals that the corresponding characteristic orbital consists of a single point at $(x, z) = (\lambda/2, 1/2)$. Substituting $D = 1$ and $z = 1/2$ into the right side of Equation 25 results in $dz/dt = 0$, giving $z_0 = z$.

3.1.4. Solutions for C and T

Combining the results from Sections 3.1.2 and 3.1.3, we obtain

$$z_0 = \begin{cases} z, & \text{if } z = \{0, 1\} \text{ or } (x, z) = (\lambda/2, 1/2), \\ \frac{1}{\pi}\operatorname{arccot}(Z_0), & \text{if } x = \{0, \lambda\} \text{ and } Z_0 \geq 0, \\ 1 + \frac{1}{\pi}\operatorname{arccot}(Z_0), & \text{if } x = \{0, \lambda\} \text{ and } Z_0 < 0, \\ \frac{1}{\pi}\arccos\left[\operatorname{cn}\left\{F\left(\pi z\middle|\frac{1}{D^2}\right) - S(x)\frac{i\pi^2 D}{\lambda}\int_0^t f(t')dt'\middle|\frac{1}{D^2}\right\}\right], & \text{otherwise,} \end{cases} \tag{40}$$

which summarizes the evolution of characteristics for this problem. Equation 40 was derived along characteristics for a given D. However, a more general form of the right side may be achieved by applying the identity from Equation 21. This substitution results in a formula that applies to characteristics everywhere in the problem domain.

According to the method of characteristics, the time-dependent solution for C is expressed as a transformation of its initial condition. Following this procedure results in

$$C(x, z, t) = C_0(z_0) = \left[1 + \exp[-2k(z_I - z_0)]\right]^{-1}, \tag{41}$$

where we may use Equation 40 for the value of z_0.

Substituting Equation 16 into Equation 1 and integrating with respect to x gives

$$Ra_T T - Ra_C C = -\frac{\pi^3\left(\lambda^2 + 1\right)^2}{\lambda^3}\cos(\pi x/\lambda)\sin(\pi z)f(t) + f_B(z, t), \tag{42}$$

where $f_B(z, t)$ is an arbitrary function independent of x. Solving for T gives

$$T(x, z, t) = \frac{1}{Ra_T}\left[-\frac{\pi^3\left(\lambda^2 + 1\right)^2}{\lambda^3}\cos(\pi x/\lambda)\sin(\pi z)f(t) + f_B(z, t) + Ra_C C\right]. \tag{43}$$

We now aim to select $f_B(z, t)$ to satisfy the isothermal boundary conditions for T at $z = 0$ and $z = 1$. Due to impermeability at the boundaries, the initial condition results in $C(x, z = 0, t) = C_0(0)$ and $C(x, z = 1, t) = C_0(1)$.

Therefore, we may select $f_B = (\mathrm{Ra}_T - \mathrm{Ra}_C)\,(1 - z)$ to ensure that $T(x, z = 0, t) = T_{\mathrm{bot}}$ and $T(x, z = 1, t) = T_{\mathrm{top}}$ (see Section 2.2.2). This gives

$$T(x, z, t) = \frac{1}{Ra_T}\left[-\frac{\pi^3\left(\lambda^2 + 1\right)^2}{\lambda^3}\cos(\pi x/\lambda)\sin(\pi z) f(t) + Ra_C C + (Ra_T - Ra_C)(1 - z)\right]. \tag{44}$$

Furthermore, it can be verified that $\partial T/\partial x = 0$ at $x = 0$ and $x = 1$. This requires showing that $\partial C/\partial x = 0$ at $x = 0$ and $x = 1$ and may be done using the symmetry of z_0 about those boundaries. This symmetry can be established using Equation 33 and noting that D is symmetric about the sidewalls. Accordingly, T satisfies both isothermal conditions at the horizontal boundaries and insulating conditions at the vertical boundaries.

3.1.5. Determining the Expression for H

Once the time-dependent solution with suitable boundary conditions is known, we may use Equation 3 to solve for H giving

$$H(x, z, t) = \frac{\partial T}{\partial t} + \mathbf{v}\cdot\nabla T - \nabla^2 T. \tag{45}$$

Explicit evaluation of Equation 45 is formidable due to a large number of terms. To this end, a Maple™ (Maple 2022, 2022) script has been used to perform the symbolic computations required. Routines that calculate $H(x, z, t)$ based upon the formula derived using Maple™ are available in Fortran and Python on GitHub and Zenodo (see Data Availability Statement for details).

3.2. Benchmark Quantities

Equation 11 can be used in conjunction with Equation 2 to compute the RMS velocity as

$$v_{\mathrm{RMS}}(t) = \frac{\pi\sqrt{\lambda^2 + 1}}{2\,\lambda}|f(t)|. \tag{46}$$

The v_{RMS} only depends on λ and $f(t)$, which are both known a priori. Accordingly, v_{RMS} does not explicitly depend on the evolution of C, T, or H.

The entrainment, given by Equation 12 with Equation 41 as the integrand, is more difficult to calculate. We were unable to find a closed-form solution. The next best alternative is to perform numerical integration, which introduces a small amount of numerical error due to spatial discretization. However, the result does not suffer from accumulation of error over time because temporal discretization is not required. In this paper, we use the composite midpoint rule for the numerical integration of entrainment. Both the RMS velocity and the entrainment may be used for benchmarking purposes.

3.3. Sample Results

3.3.1. Temporally Periodic Flow

In this example, we present a flow that is periodic in time. Sample plots of temperature, composition, and internal heating rate using $f(t) = a\sin(\pi bt)$ with $\lambda = 1$, $a = 100$, $b = 100$, $z_l = 0.5$, $k = 35$, and $\mathrm{Ra}_T = 1 \times 10^5$ are shown in Figure 2, where the buoyancy ratio is given by $B = \mathrm{Ra}_C/\mathrm{Ra}_T$. At $t = 0$, there are no lateral variations in buoyancy, corresponding to a velocity field of zero throughout the domain. Lateral gradients in thermal buoyancy are generated by the internal heating rate, which starts the flow for $t > 0$. At $t = 0.005$, we have a hot upwelling of compositionally dense material on the right and a cold downwelling of ambient material on the left, resulting from counterclockwise flow. At $t = 0.01$, the counterclockwise flow has caused the compositionally dense material to descend through the left portion of the domain. Correspondingly, the ambient material has ascended through the right portion of the domain, resulting in a "jelly roll" pattern. The temperature fields for buoyancy ratios of 0.5 and 1 are similar in character overall. However, there is an additional thermal gradient in z throughout the domain for the $B = 0.5$ case, due to the term $(\mathrm{Ra}_T - \mathrm{Ra}_C)\,(1 - z)/\mathrm{Ra}_T$ in Equation 44. For $B = 1$, we have $\mathrm{Ra}_T = Ra_C$ which nullifies the contribution of that term.

We also observe thin columns of hot compositionally dense and cold compositionally buoyant material for $t > 0$ along the bottom right and top left sides, respectively. These sharp gradients of C and T are due to impermeable

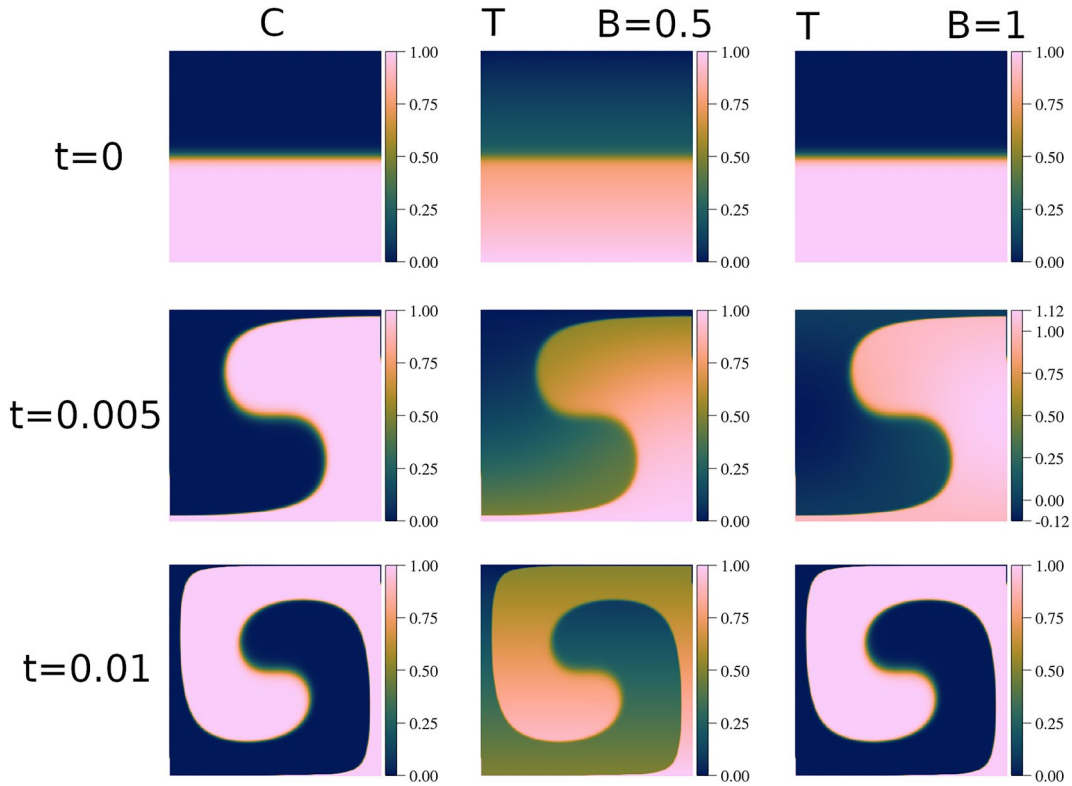

Figure 2. Plots of C and T using $f(t) = a\sin(\pi bt)$ with $\lambda = 1$, $a = 100$, $b = 100$, $z_I = 0.5$, $k = 35$, and $\mathrm{Ra}_T = 1 \times 10^5$. Temperature snapshots for buoyancy ratio values of 0.5 and 1.0 are shown. Time values are given in the leftmost portion of the figure.

boundary conditions and a lack of diffusion. Impermeability results in boundary material being trapped along its boundary. Also, the velocity of boundary material approaches zero as the domain corners are approached. This leads to the side wall material lagging behind nearby material in the domain interior, generating sharp gradients. In addition to zero compositional diffusivity, H exactly cancels thermal diffusion (see Equation 45 and Section 4.4). Accordingly, the absence of diffusion preserves the sharp gradients in C and T near the side walls.

Snapshots of H corresponding to the cases shown in Figure 2 are presented in Figure 3. Due to the range of H values for these plots, a symmetric log scale was used for the color scale for internal heating magnitudes greater than unity. For $-1 < H < 1$, a linear color mapping is used to avoid difficulties that a log scale would encounter near $H = 0$.

The internal heating rate impacts the thermal buoyancy so that the resulting velocity field is consistent with the assumed stream function in Equation 16. At $t = 0$, H encourages counterclockwise flow in the upper and lower portions of the domain. However, counterclockwise flow is inhibited near the material interface, resulting in a low-velocity counterclockwise flow to start. At $t = 0.005$, H enhances counterclockwise flow in most of the domain, resulting in vigorous flow. Finally, at $t = 0.01$, H acts to generate clockwise flow because the choice of $f(t)$ leads to a flow reversal at this time. For $t = 0$ and 0.01, the behavior of H is quite similar for $B = 0.5$ and 1. However, for $t = 0.005$, long wavelength H gradients independent of the compositional interface differ between $B = 0.5$ and 1.

Plots of the velocity components and magnitude in terms of λ and $f(t)$ are shown in Figure 4. For this sample problem, the leftmost column (i.e., $\lambda = 1$) applies, where the extreme values of u, w, and $|\mathbf{v}|$ depend on the value of $f(t)$.

The exact RMS velocity and approximate entrainment values corresponding to the selected parameters are shown in Figure 5. Due to the choice of $f(t)$, the velocity field is temporally periodic and has zero magnitude at times 0 and 0.01.

The initial entrainment is slightly above zero due to the reference z value ($z_R = z_I$) being situated in the center of the compositional interface. Accordingly, there is a small amount of dense material that is already above z_R at $t = 0$. Subsequently, the entrainment steadily rises to a peak value of approximately 0.7388 at $t = 0.0062$. Afterward, the head of the compositionally dense region begins to descend below z_R, leading to a decrease in entrainment. Finally, the entrainment value at $t = 0.01$ is approximately 0.5903.

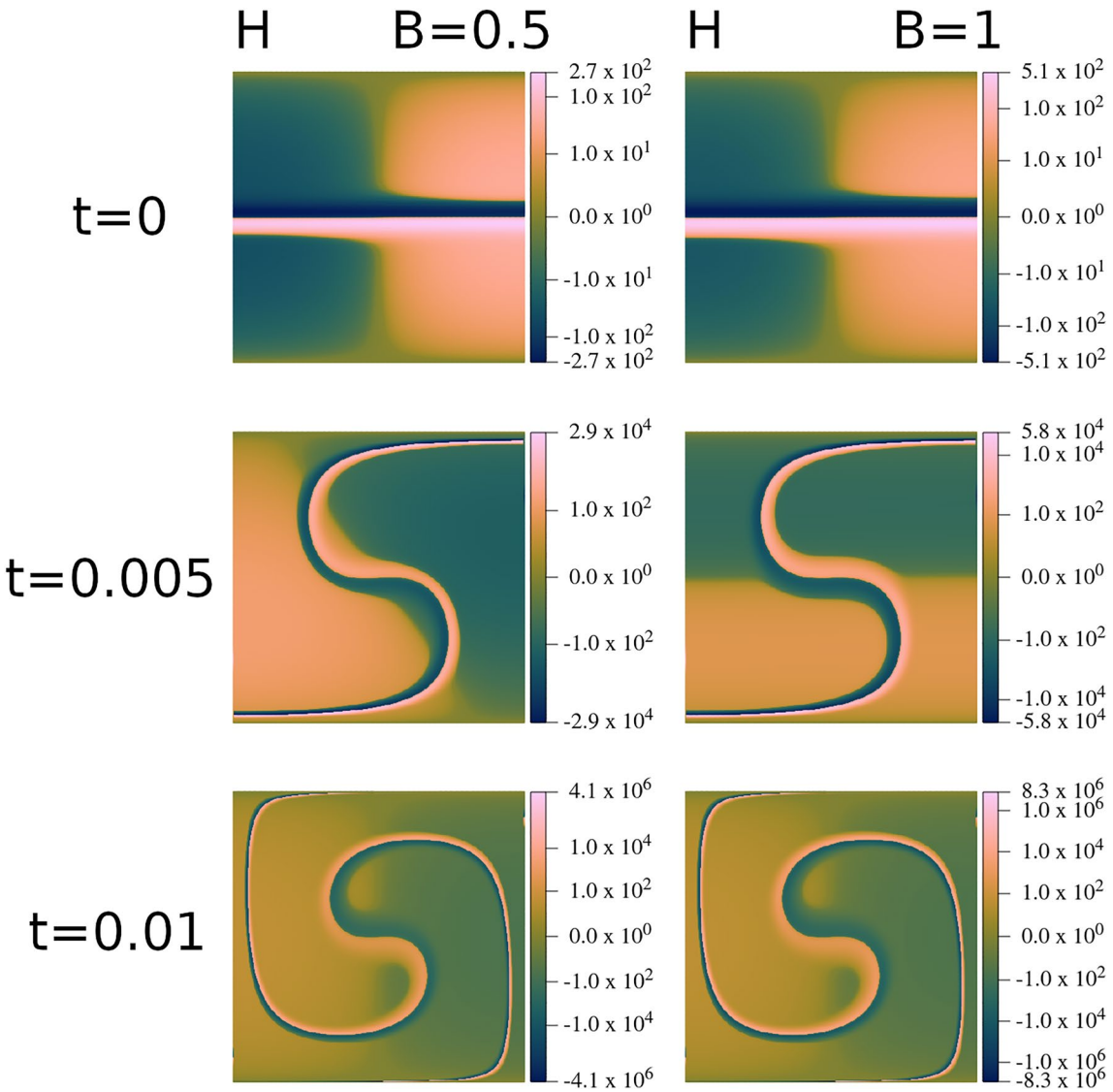

Figure 3. Plots of H using $f(t) = a\sin(\pi bt)$ with $\lambda = 1$, $a = 100$, $b = 100$, $z_1 = 0.5$, $k = 35$, and $\mathrm{Ra}_T = 1 \times 10^5$ are shown for buoyancy ratio values of 0.5 and 1.0. Time values are given in the leftmost portion of the figure. Note that a symmetric log scale is used for the color bar, except for $-1 < H < 1$, where a linear color mapping is used.

We have selected the above parameters to be approximately consistent with a thermochemical mantle convection model with a thermal Rayleigh number of 10^5. For instance, for the same domain and boundary conditions, the RMS velocity of purely thermal convection at steady state has been observed to be under 200 units (see case 1b from Blankenbach et al. (1989)). The mean RMS velocity for our sample parameters is $100\sqrt{2} \approx 141.4$ units, which may be reasonable given that half the domain contains intrinsically dense material.

3.3.2. Approaching a Steady State

In contrast to the example shown in Section 3.3.1, we now present a case that approaches a steady state flow. Specifically, we use $f(t) = a\sin(\pi bt)e^{-ct} + d$ with $\lambda = 3/2$, $a = 600/(\pi\sqrt{13})$, $b = 100$, $c = 50$, $d = 4500/(\pi\sqrt{13})$, $z_1 = 0.2$, $k = 35$, $\mathrm{Ra}_T = 1 \times 10^6$, and $\mathrm{Ra}_C = 8 \times 10^5$. Figure 6 shows snapshots of C and T for several time values between 0 and 0.1. At $t = 0$, the solution begins with a basal layer of hot compositionally dense material that is 0.2 units thick. Subsequently, the basal layer begins to undergo shearing in a counterclockwise direction. Early evolution of C for $t = 0$ to $t = 0.005$ is shown in Figure 7, where we observe the transformation of the initial dense layer into a spiraling band due to rotational shear. Unlike Section 3.3.1, the flow continues in a counterclockwise direction as time elapses. By $t = 0.025$ (Figure 6), the dense material has been sheared into a spiral pattern. The

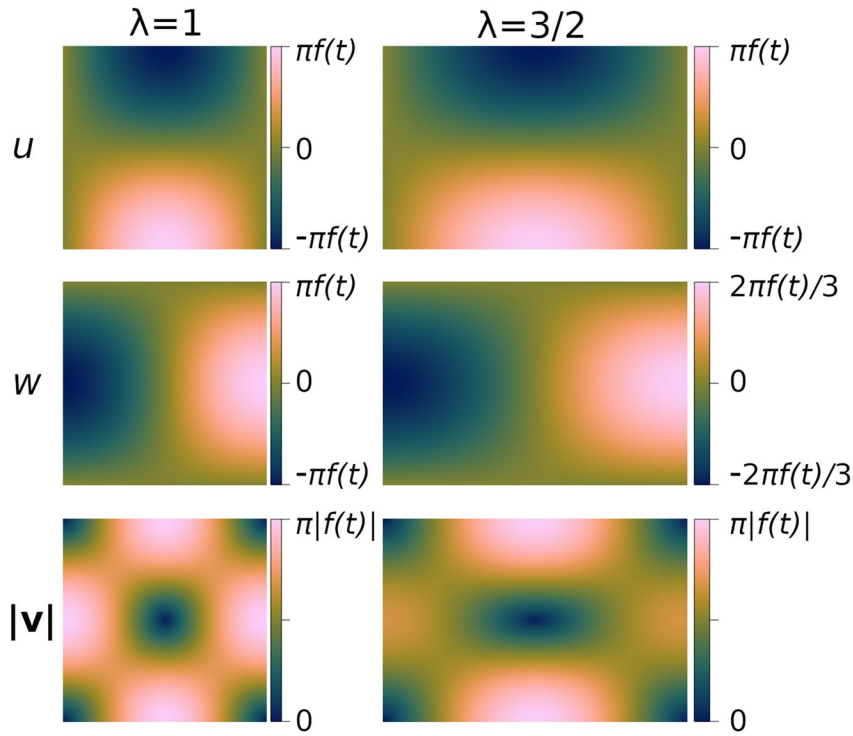

Figure 4. Plots of u, w, and $|\mathbf{v}|$ for $\lambda = 1$ and $\lambda = 3/2$. Note that the color scale bounds depend on $f(t)$.

number of spiral turns is proportional to the number of mantle overturns. This quantity can be estimated by integrating the RMS velocity with respect to time, which estimates the number of transits across the depth of the mantle, and dividing by four. For $t = 0.025$, we have approximately five overturns. By $t = 0.05$, nearly 10 overturns have occurred, corresponding to an increase in spiral turns. Continued shearing results in thinning of the spiral layer. By $t = 0.075$, we have approximately 14 overturns, with a further decrease in spiral layer thickness. Finally, by $t = 0.1$, approximately 19 overturns have occurred and the flow is near a steady state. The spiral layer has become even thinner due to shearing.

It is interesting to note that compositionally dense material is localized to the outer perimeter of the domain, even as t approaches infinity. Specifically, the dense material cannot pass the characteristic orbital given by the largest value of D within the basal layer at $t = 0$; the orbital barrier is given by $D = \sin(\pi z_l) \approx 0.588$ (see Figure 1 for reference). Strictly speaking, this D value holds for $C > 0.5$ because we used the center of the initial compositional interface in our calculation. The orbital barrier for the remaining dense material corresponds to a slightly larger D, due to the thickness of the compositional interface at $t = 0$.

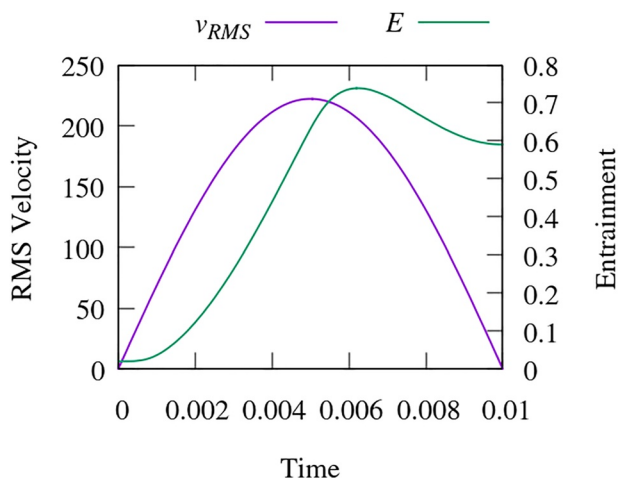

Figure 5. Plots of v_{RMS} and E using $f(t) = a\sin(\pi bt)$ with $\lambda = 1$, $a = 100$, $b = 100$, $z_l = 0.5$, $k = 35$, and $\mathrm{Ra}_T = 1 \times 10^5$. The entrainment was calculated using the composite midpoint rule with a uniformly spaced 401×401 grid.

Snapshots of H for the same times in Figure 6 are shown in Figure 8. Here H can be described as a superposition of features corresponding to (a) the compositional layer and (b) a long wavelength gradient stemming from terms independent of C in Equation 44. For all times shown, the long wavelength component introduces asymmetry that promotes counterclockwise flow. For $t = 0$, we observe that compositionally dense material is heated internally between $x = 0$ and $x \approx 2\lambda/3$, while material just above the interface is cooled internally. At $t = 0.025$, we observe that the dense material spiral is heated near the compositional interface, while the less compositionally dense material just beyond the interface is cooled. This trend holds for $t \geq 0.025$ but becomes less pronounced as time increases. We also note that the innermost spirals in H are located closer to the domain center than those of C or T (see Figure 6). The H spirals corresponding to $D > 0.588$ only impact material

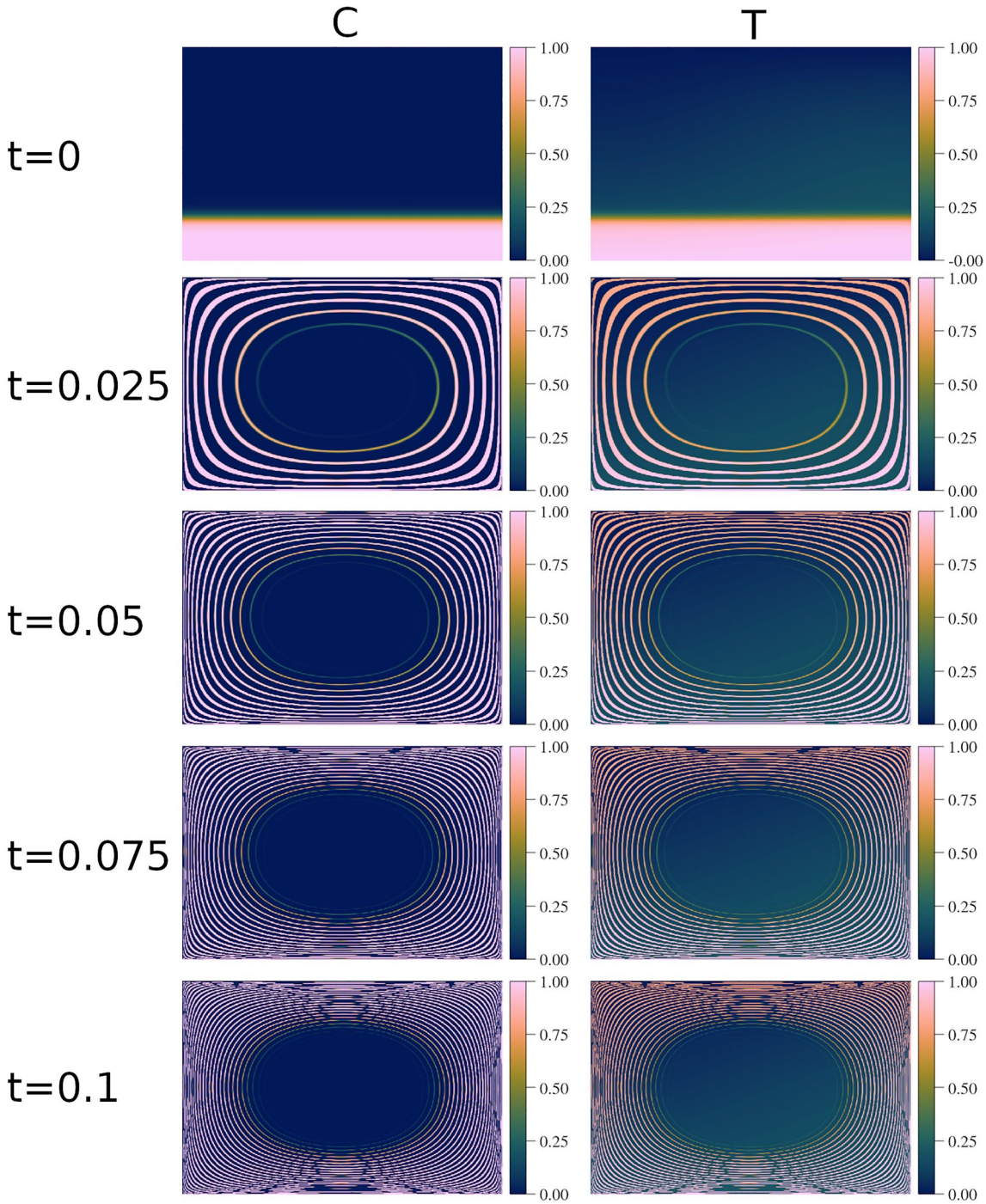

Figure 6. Plots of C and T using $f(t) = a\sin(\pi bt)e^{-ct} + d$ with $\lambda = 3/2$, $a = 600/(\pi\sqrt{13})$, $b = 100$, $c = 50$, $d = 4500/(\pi\sqrt{13})$, $z_l = 0.2$, $k = 35$, $\mathrm{Ra}_T = 1 \times 10^6$, and $\mathrm{Ra}_C = 8 \times 10^5$. Time values are given in the leftmost portion of the figure.

with $C < 0.5$ (with the majority near or at $C = 0$). For $t \in [0.05, 0.1]$, the spiral band becomes thinner as time elapses, similar to C and T. In addition, it is observed that the innermost position of the spiral band does not change significantly.

As before, Figure 4 shows the velocity components and magnitude in terms of λ and $f(t)$. For this problem, the rightmost column in the figure (i.e., $\lambda = 3/2$) applies, where extreme values of u, w, and $|\mathbf{v}|$ depend on the value of $f(t)$.

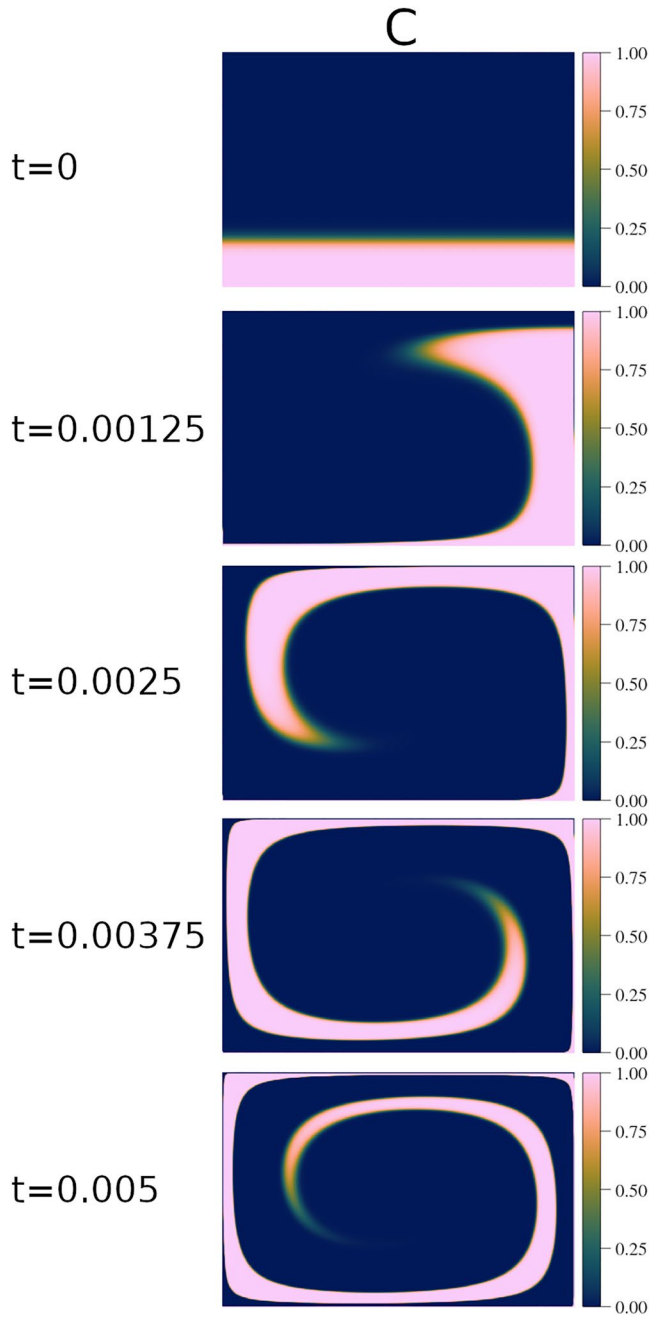

Figure 7. Plots of C at early stages of evolution using $f(t) = a\sin(\pi bt)e^{-ct} + d$ with $\lambda = 3/2$, $a = 600/(\pi\sqrt{13})$, $b = 100$, $c = 50$, $d = 4500/(\pi\sqrt{13})$, $z_I = 0.2$, $k = 35$, $\mathrm{Ra}_T = 1 \times 10^6$, and $\mathrm{Ra}_C = 8 \times 10^5$. Time values are given in the leftmost portion of the figure.

Figure 9 shows the exact RMS velocity and the approximate entrainment versus time for this sample problem. The RMS velocity gradually approaches a steady-state value of 750 units. As time increases, the RMS velocity oscillates with decreasing amplitude about the steady-state value. The steady-state RMS velocity value was selected (via d) to be a bit less than that observed in previous benchmarks for thermal mantle convection (see problem 1c from Blankenbach et al. (1989)). It was presumed that the presence of dense material consisting of 20% of the domain volume would result in a decreased RMS velocity.

As in Section 3.3.1, the initial entrainment is slightly above zero due to z_R being situated in the center of the compositional interface. The entrainment sharply increases until reaching a peak value of approximately 0.9575

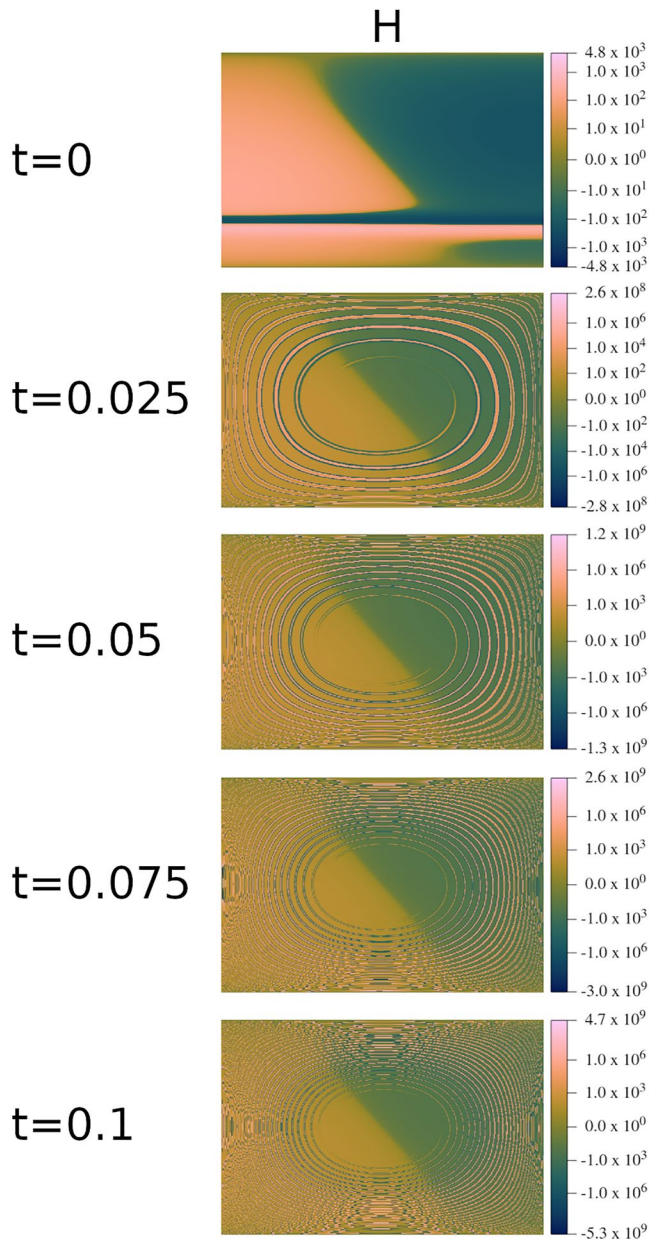

Figure 8. Plots of H using $f(t) = a\sin(\pi bt)e^{-ct} + d$ with $\lambda = 3/2$, $a = 600/(\pi\sqrt{13})$, $b = 100$, $c = 50$, $d = 4500/(\pi\sqrt{13})$, $z_l = 0.2$, $k = 35$, $\mathrm{Ra}_T = 1 \times 10^6$, and $\mathrm{Ra}_C = 8 \times 10^5$. Time values are given in the leftmost portion of the figure. A symmetric log scale is used for the color bar, except for $-1 < H < 1$, where a linear color mapping is used.

at $t = 0.0025$ (C shown in Figure 7). Following that, the entrainment quickly reaches a quasi steady state beyond about $t = 0.02$ with an average entrainment value of 0.6923. During that period, the amount of dense material that is transported above z_R nearly matches the amount of dense material that descends below z_R.

4. Discussion

4.1. Use in Mantle Convection Codes

In this study, we have manufactured an exact solution for a problem that can be set up in many mantle convection codes. We now discuss the necessary steps for code setup to generate numerical solutions for comparison with the manufactured solution presented in this paper. The setup steps are as follows:

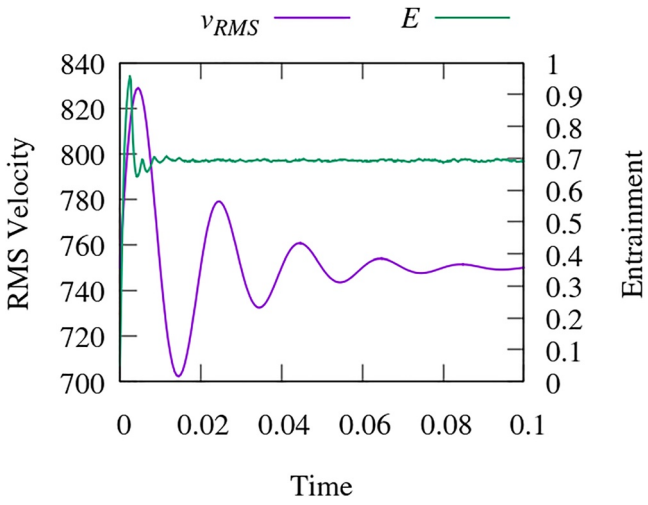

Figure 9. Plots of v_{RMS} and E using $f(t) = a\sin(\pi bt)e^{-ct} + d$ with $\lambda = 3/2$, $a = 600/(\pi\sqrt{13})$, $b = 100$, $c = 50$, $d = 4500/(\pi\sqrt{13})$, $z_l = 0.2$, $k = 35$, $\mathrm{Ra}_T = 1 \times 10^6$, and $\mathrm{Ra}_C = 8 \times 10^5$. The entrainment was calculated using the composite midpoint rule with a uniformly spaced 751×501 grid.

1. Select values for physical constants λ, z_l, k, Ra_T, and Ra_C.
2. Select a function $f(t)$ and values for any associated parameters (e.g., a and b for $f(t) = a\sin(\pi bt)$).
3. Set initial conditions according to Section 2.2.1.
4. Set boundary conditions according to Section 2.2.2.
5. Set the internal heating rate according to the routines provided via GitHub/Zenodo (see Data Availability Statement for details).

After these setup steps are complete, the model can be run forward in time with the settings that require testing (e.g., resolution, particle count, time integration scheme, etc.). We note that time accuracy can be precisely quantified using the derived solutions; the inability to precisely quantify time accuracy has been a challenge for thermochemical convection codes (van Keken et al., 1997).

Steps 1–3 are straightforward. For particle methods, step 4 may pose a challenge in terms of setting up the initial condition for C due to the requirement of a specific thickness and gradient in the compositional interface. If particles track both compositions (e.g., the ratio method outlined in Tackley and King (2003)) and can support intermediate C values between 0 and 1, the interface can be precisely set using Equation 7. However, if only one composition is tracked (e.g., the absolute method described in van Keken et al. (1997) and Tackley and King (2003)) or particles do not support intermediate C values, Equation 7 is more difficult to satisfy for the interface. One possibility is to select k so that the initial interface thickness matches that which is available in the code. However, this does not guarantee that the gradient of C will match that of Equation 7. This limitation may lead to discrepancies between the numerical and manufactured solutions. In addition, initializing particles along the domain boundaries may help to resolve the sharp gradients observed there.

Step 5 may also require some extra programming if internal heating rates that vary in space and time are not available in the code of interest. For a successful test, the variable internal heating rate must be updated sufficiently often in the code (e.g., once per stage of a Runge–Kutta time integration scheme).

To calculate H correctly, numerical implementations of elliptic integrals of the first and second kinds are required and must allow a Jacobi amplitude range of at least $[0, \pi]$. Additionally, implementations of the Jacobi elliptic functions (sn, cn, dn) must permit complex first arguments. Both the elliptic integral and Jacobi elliptic functions must allow elliptic parameter values greater than unity. We note that this functionality is not standard in all software packages. However, the Fortran (and Python) routines provided in the Data Availability Statement satisfy these requirements by applying generalizations to the algorithms presented in Fukushima (2012, 2013).

Due to a large number of terms and relatively expensive function evaluations for F and cn, the calculation of H may be non-trivial. Because H takes the form of a source term in Equation 3 and is time varying, it needs to be evaluated each time the numerical method makes a right-hand side function evaluation. This may adversely impact the computation time required to generate numerical approximations to the exact solution.

We note that T values can be negative or exceed unity in the solution. Accordingly, numerical schemes must allow such values for T. Also, codes must allow top and bottom boundary temperatures other than zero and unity for best results (see Section 2.2.2).

4.2. Testing With a Convection Code

In this section, we test the functionality of the software used to compute H with the convection code ProjecTracer (S. J. Trim et al., 2020). The code features a particle-in-cell method for the advection of both temperature and composition, while velocity (via a stream function formulation) and thermal diffusion are computed on an Eulerian mesh using centered finite differences. Our calculations were produced using a uniform Eulerian mesh consisting of $n \times n$ (n ranges between 200 and 800) cells with fourth-order finite differences. Each Eulerian dual grid cell was initialized with 60 tracer particles and bilinear shape functions were used to interpolate

particle values to the Eulerian grid. Time integration was performed using the explicit two-stage, second-order midpoint Runge–Kutta method with a Courant factor of 0.99. We consider the temporally periodic problem from Section 3.3.1 with $B = 0.5$.

Figure 10 shows a comparison between numerical and exact solutions for C, T, and ψ at $t = 0.0025$ for $n = 800$. We observe that the numerical results generally match the exact solution. However, the numerical solution did not capture the sharp gradients near the domain boundaries for C and T in the exact solution. This may be due to an overestimation of thermal diffusion at the boundaries in the numerical solution. Placing tracer particles specifically on the domain boundaries improved accuracy in the numerical results. However, it is expected that mesh refinement near the boundaries would improve accuracy further. Also, the magnitude of ψ

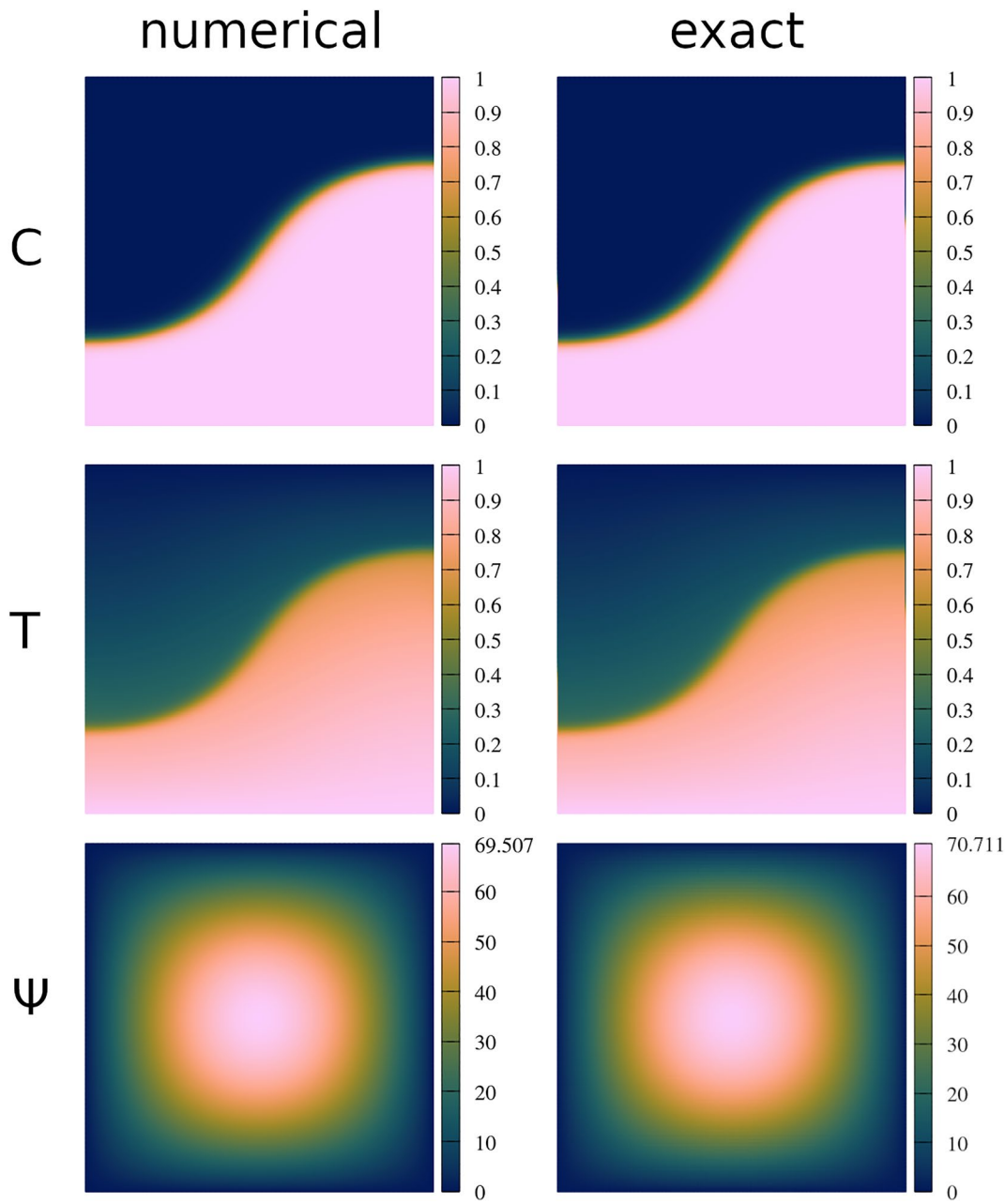

Figure 10. Snapshots of C, T, and ψ at $t = 0.0025$ using $f(t) = a\sin(\pi bt)$ with $\lambda = 1$, $a = 100$, $b = 100$, $z_l = 0.5$, $k = 35$, $\mathrm{Ra}_T = 1 \times 10^5$, and $\mathrm{Ra}_C = 0.5 \times 10^5$. Numerical results computed using ProjecTracer are shown in the left column, and exact solutions are shown in the right column.

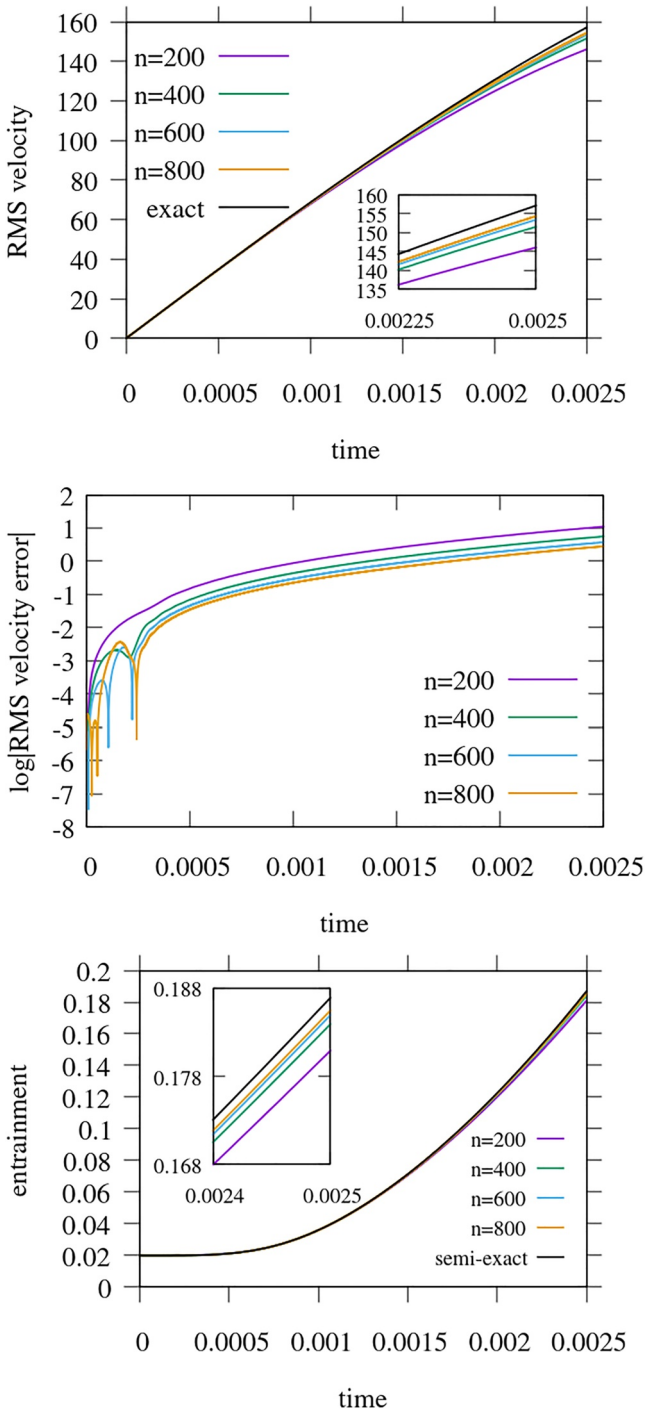

Figure 11. Time series of v_{RMS}, the logarithm of the v_{RMS} error magnitude, and the entrainment using $f(t) = a\sin(\pi bt)$ with $\lambda = 1$, $a = 100$, $b = 100$, $z_l = 0.5$, $k = 35$, $\mathrm{Ra}_T = 1 \times 10^5$, and $\mathrm{Ra}_C = 0.5 \times 10^5$. Results were obtained using ProjecTracer with a $n \times n$ Eulerian mesh, where n is given in the plot legends. Inset plots are shown for a more precise view of final evolution. For v_{RMS}, the exact solution is shown for reference. For entrainment, a semi-exact curve is shown for reference, calculated by applying the composite midpoint rule with a uniform 800×800 mesh according to Section 3.2.

is underestimated in the numerical solution, likely due to the accumulation of error over time.

Figure 11 shows time series of v_{RMS}, the logarithm of the v_{RMS} error magnitude, and the entrainment for different values of n. We observe that the numerical solutions approach the exact (or semi-exact in the case of entrainment as in Section 3.2) solution as n increases. For the time interval considered, errors may be within an acceptable tolerance, particularly for large n. However, error is observed to accumulate over time. Accordingly, for longer integration times it may be a challenge to maintain an acceptable error tolerance. This is a common occurrence in practice due to a combination of many factors including sensitivity of the equations, the numerical method employed, and floating-point arithmetic. In such situations, increasing the spatial resolution or decreasing the time step size may lead to improved results.

4.3. Thickness of the Compositional Interface

The interface thickness between distinct compositions must be non-zero for the internal heating rate to remain bounded. For example, if the Heaviside function is used to specify the initial condition for C, then H contains terms including the Dirac delta function and its derivatives. This poses a challenge for convection codes because it is not practical to implement an internal heating rate that is not bounded. For these reasons, we have selected a smooth approximation to the Heaviside function for the initial condition for C. However, with a sufficiently large k value, the interface thickness can in principle be made as sharp as needed.

4.4. The Sharpness of Temperature Contrasts

In situations where the stream function (or velocity field) is smooth, gradients in temperature are of similar sharpness to those of composition. This similarity can be seen by examining Equation 1. This is also the case for our manufactured solution and can be seen in Figure 2.

Additionally, from Equation 45 it is observed that H is partially comprised of a negative diffusion term. Accordingly, H contributes to the sharpness of temperature gradients in the exact solution.

Therefore, the numerical method used for the advection-diffusion equation for temperature should be capable of handling sharp gradients. One possibility is to apply particle methods for temperature in a similar fashion to their use for composition (Gerya & Yuen, 2003; S. J. Trim et al., 2020).

4.5. Extension to 3D

Extension of the derivation to 3D would also provide a useful test of code accuracy and correctness beyond 2D flows. However, several complexities would need to be addressed for a 3D manufactured solution, including an increased number of variables and equations. For instance, using poloidal-toroidal decomposition, we can describe the flow velocity with two scalar potentials. In that case, the 3D Stokes equation can be reduced to two scalar equations (Chandrasekhar, 2013). The determination of suitable characteristic orbitals would also be more challenging and may involve multiple parameters (as opposed to just D in the 2D case). Nonetheless, a 3D solution would be helpful for testing community codes and is worthy of future exploration.

5. Conclusions

Using the method of characteristics, a manufactured solution is derived for isoviscous 2D thermochemical mantle convection models for a prescribed stream function. Exact expressions for velocity, temperature, composition, and internal heating rate are derived. Due to the large number of terms, the expression for the internal heating rate is found using computer algebra software and is provided on GitHub and Zenodo in Maple™, Fortran, and Python (see Data Availability Statement). The solution features a non-stationary velocity field, thermal and compositional buoyancy effects, and a sharp compositional interface. The method of characteristics facilitates a solution without additional diffusion or source terms in the compositional transport equation, allowing the preservation of sharp compositional interfaces in time and space. For the problem posed, the sharpness of temperature contrasts is similar to that of composition. The exact solution can be used to test the correctness and accuracy of thermochemical mantle convection codes and allows precise evaluation of the accuracy of numerical solutions for all problem variables in time and space.

Data Availability Statement

Software-related files and data supporting this article are maintained on GitHub (https://github.com/seantrim/exact-thermochem-solution) and archived on Zenodo (S. Trim, 2023a). Files include a computer algebra script for Maple™ (Maple 2022, 2022) that was used for the symbolic computation of H. In addition, Fortran files containing the formula for H, translated from Maple™ results, and related functions/routines are provided. Scripts for Python compatibility are also available. Calculations in Section 4.2 were performed using ProjecTracer, available on GitHub (https://github.com/seantrim/ProjecTracer) and Zenodo (S. Trim, 2023b).

Figures in this article were made using SageMath (The Sage Developers, 2022), Gnuplot (Williams & Kelley, 2021), GIMP (GIMP: GNU Image Manipulation Program, 2021), and MATLAB® (MATLAB, 2022). SageMath (https://www.sagemath.org), Gnuplot (http://www.gnuplot.info), and GIMP (https://www.gimp.org) are available via free licenses. Plots of C, T, and H were made using the perceptually uniform batlow color map (Crameri et al., 2020) and is available on Zenodo (Crameri, 2021). Maple™ (https://www.maplesoft.com) and MATLAB® (https://www.mathworks.com) have commercial licenses but are often available through institutional access. Maple™ is a trademark of Waterloo Maple Inc.

Acknowledgments

We would like to thank Henri Samuel and Cedric Thieulot for thoughtful reviews. S.J.T, S.S.C.M, and R.J.S are grateful for funding from the Natural Sciences and Engineering Research Council of Canada under its Discovery Grant Program (RGPN-2020-04467 (R.J.S)) and Undergraduate Student Research Award Program (S.S.C.M.). S.L.B is also grateful for funding from the Natural Sciences and Engineering Research Council of Canada (RGPN-2020-06332).

References

Batchelor, G. (1967). An introduction to fluid dynamics (p. 615). UP xviii.

Blankenbach, B., Busse, F., Christensen, U., Cserepes, L., Gunkel, D., Hansen, U., et al. (1989). A benchmark comparison for mantle convection codes. *Geophysical Journal International*, *98*(1), 23–38. https://doi.org/10.1111/j.1365-246x.1989.tb05511.x

Brunton, S. L., & Rowley, C. W. (2010). Fast computation of finite-time Lyapunov exponent fields for unsteady flows. *Chaos: An Interdisciplinary Journal of Nonlinear Science*, *20*(1), 017503. https://doi.org/10.1063/1.3270044

Chandrasekhar, S. (2013). *Hydrodynamic and hydromagnetic stability*. Courier Corporation.

Courant, R., & Hilbert, D. (2008). *Methods of mathematical physics: Partial differential equations*. John Wiley & Sons.

Crameri, F. (2021). Scientific colour maps. *Zenodo*. (The development of the Scientific colour maps is not funded any longer, but will continue as a pro bono project for the scientific community. - Fabio). https://doi.org/10.5281/zenodo.5501399

Crameri, F., Shephard, G. E., & Heron, P. J. (2020). The misuse of colour in science communication. *Nature Communications*, *11*(1), 5444. https://doi.org/10.1038/s41467-020-19160-7

Davies, D., Goes, S., & Lau, H. (2015). Thermally dominated deep mantle LLSVPs: A review. *The Earth's Heterogeneous Mantle: A Geophysical, Geodynamical, and Geochemical Perspective*, 441–477. https://doi.org/10.1007/978-3-319-15627-9_14

De Smet, J. H., Van Den Berg, A. P., Vlaar, N. J., & Yuen, D. A. (2000). A characteristics-based method for solving the transport equation and its application to the process of mantle differentiation and continental root growth. *Geophysical Journal International*, *140*(3), 651–659. https://doi.org/10.1046/j.1365-246x.2000.00993.x

Duretz, T., May, D. A., Gerya, T., & Tackley, P. (2011). Discretization errors and free surface stabilization in the finite difference and marker-in-cell method for applied geodynamics: A numerical study. *Geochemistry, Geophysics, Geosystems*, *12*(7), Q07004. https://doi.org/10.1029/2011gc003567

Enright, D., Fedkiw, R., Ferziger, J., & Mitchell, I. (2002). A hybrid particle level set method for improved interface capturing. *Journal of Computational Physics*, *183*(1), 83–116. https://doi.org/10.1006/jcph.2002.7166

Fukushima, T. (2012). Precise and fast computation of a general incomplete elliptic integral of third kind by half and double argument transformations. *Journal of Computational and Applied Mathematics*, *236*(7), 1961–1975. https://doi.org/10.1016/j.cam.2011.11.007

Fukushima, T. (2013). Precise and fast computation of Jacobian elliptic functions by conditional duplication. *Numerische Mathematik*, *123*(4), 585–605. https://doi.org/10.1007/s00211-012-0498-0

Gassmöller, R., Lokavarapu, H., Bangerth, W., & Puckett, E. G. (2019). Evaluating the accuracy of hybrid finite element/particle-in-cell methods for modelling incompressible Stokes flow. *Geophysical Journal International*, *219*(3), 1915–1938. https://doi.org/10.1093/gji/ggz405

Gerya, T. V., & Yuen, D. A. (2003). Characteristics-based marker-in-cell method with conservative finite-differences schemes for modeling geological flows with strongly variable transport properties. *Physics of the Earth and Planetary Interiors*, *140*(4), 293–318. https://doi.org/10.1016/j.pepi.2003.09.006

GIMP: GNU Image Manipulation Program. (2021). version 2.10.30. Retrieved from https://www.gimp.org
Hillebrand, B., Thieulot, C., Geenen, T., Van Den Berg, A., & Spakman, W. (2014). Using the level set method in geodynamical modeling of multi-material flows and Earth's free surface. *Solid Earth*, *5*(2), 1087–1098. https://doi.org/10.5194/se-5-1087-2014
Kellogg, L., & Turcotte, D. (1990). Mixing and the distribution of heterogeneities in a chaotically convecting mantle. *Journal of Geophysical Research*, *95*(B1), 421–432. https://doi.org/10.1029/jb095ib01p00421
Lenardic, A., & Kaula, W. (1993). A numerical treatment of geodynamic viscous flow problems involving the advection of material interfaces. *Journal of Geophysical Research*, *98*(B5), 8243–8260. https://doi.org/10.1029/92jb02858
Maple 2022. (2022). *Maplesoft, a division of Waterloo Maple Inc*. Waterloo Maple Inc. Retrieved from https://www.maplesoft.com
MATLAB. (2022). *Version 9.12.0 (r2022a)*. The MathWorks Inc. Retrieved from https://www.mathworks.com
McNamara, A. K. (2019). A review of large low shear velocity provinces and ultra low velocity zones. *Tectonophysics*, *760*, 199–220. https://doi.org/10.1016/j.tecto.2018.04.015
Pusok, A. E., Kaus, B. J., & Popov, A. A. (2017). On the quality of velocity interpolation schemes for marker-in-cell method and staggered grids. *Pure and Applied Geophysics*, *174*(3), 1071–1089. https://doi.org/10.1007/s00024-016-1431-8
Samuel, H. (2018). A deformable particle-in-cell method for advective transport in geodynamic modelling. *Geophysical Journal International*, *214*(3), 1744–1773. https://doi.org/10.1093/gji/ggy231
Samuel, H., & Evonuk, M. (2010). Modeling advection in geophysical flows with particle level sets. *Geochemistry, Geophysics, Geosystems*, *11*(8). https://doi.org/10.1029/2010gc003081
Schubert, G., Turcotte, D. L., & Olson, P. (2001). *Mantle convection in the Earth and planets*. Cambridge University Press.
Tackley, P. J., & King, S. D. (2003). Testing the tracer ratio method for modeling active compositional fields in mantle convection simulations. *Geochemistry, Geophysics, Geosystems*, *4*(4), 8302. https://doi.org/10.1029/2001gc000214
The Sage Developers. (2022). Sagemath, the sage mathematics software system (version 9.5). [Computer software manual]. Retrieved from https://www.sagemath.org
Trim, S. (2023a). seantrim/exact-thermochem-solution: Release 1.2.0. *Zenodo*. https://doi.org/10.5281/zenodo.7671498
Trim, S. (2023b). seantrim/projectracer: Release 1.2.0. *Zenodo*. https://doi.org/10.5281/zenodo.7671666
Trim, S. J., Butler, S. L., & Spiteri, R. J. (2021). Benchmarking multiphysics software for mantle convection. *Computers & Geosciences*, *154*, 104797. https://doi.org/10.1016/j.cageo.2021.104797
Trim, S. J., Lowman, J. P., & Butler, S. L. (2020). Improving mass conservation with the tracer ratio method: Application to thermochemical mantle flows. *Geochemistry, Geophysics, Geosystems*, *21*(2), e2019GC008799. https://doi.org/10.1029/2019gc008799
Turcotte, D. L., & Schubert, G. (2002). *Geodynamics*. Cambridge University Press.
van Keken, P., King, S., Schmeling, H., Christensen, U., Neumeister, D., & Doin, M.-P. (1997). A comparison of methods for the modeling of thermochemical convection. *Journal of Geophysical Research*, *102*(B10), 22477–22495. https://doi.org/10.1029/97jb01353
Williams, T., & Kelley, C. (2021). Gnuplot 5.4: An interactive plotting program. Retrieved from http://www.gnuplot.info/
Zhong, S. (1996). Analytic solutions for Stokes' flow with lateral variations in viscosity. *Geophysical Journal International*, *124*(1), 18–28. https://doi.org/10.1111/j.1365-246x.1996.tb06349.x